Journal of the Mechanics and Physics of Solids 61 (2013) 1319–1336

Contents lists available at SciVerse ScienceDirect

Journal of the Mechanics and Physics of Solids

journal homepage: www.elsevier.com/locate/jmps

Three-dimensional numerical modeling of composite panels subjected to underwater blast

Xiaoding Wei, Phuong Tran, Alban de Vaucorbeil, Ravi Bellur Ramaswamy, Felix Latourte [1], Horacio D. Espinosa *

Department of Mechanical Engineering, Northwestern University, 2145 Sheridan Road, Evanston, IL 60208-3111, United States

A R T I C L E I N F O

Article history:
Received 14 August 2012
Received in revised form
18 February 2013
Accepted 22 February 2013
Available online 7 March 2013

Keywords:
Finite element analysis
Fluid–structure interaction
Composite failure
Underwater blast
Delamination
Foam compaction

A B S T R A C T

Designing lightweight high-performance materials that can sustain high impulsive loadings is of great interest for marine applications. In this study, a finite element fluid–structure interaction model was developed to understand the deformation and failure mechanisms of both monolithic and sandwich composite panels. Fiber (E-glass fiber) and matrix (vinylester resin) damage and degradation in individual unidirectional composite laminas were modeled using Hashin failure model. The delamination between laminas was modeled by a strain-rate sensitive cohesive law. In sandwich panels, core compaction (H250 PVC foam) is modeled by a crushable foam plasticity model with volumetric hardening and strain-rate sensitivity. The model-predicted deformation histories, fiber/matrix damage patterns, and inter-lamina delamination, in both monolithic and sandwich composite panels, were compared with experimental observations. The simulations demonstrated that the delamination process is strongly rate dependent, and that Hashin model captures the spatial distribution and magnitude of damage to a first-order approximation. The model also revealed that the foam plays an important role in improving panel performance by mitigating the transmitted impulse to the back-side face sheet while maintaining overall bending stiffness.

1. Introduction

The design and manufacture of lightweight yet stiff and strong materials has attracted a lot of attention recently due to fast-growing military and civilian needs. A number of applications require high strain-rate behavior, e.g., marine hulls subjected to underwater explosions (Porfiri and Gupta, 2010; Chen et al., 2009) or automobile parts designed for crash absorption (Lee et al., 2000; Zarei and Kröger, 2008). The use of sandwich structures (e.g., two solid face sheets with a foam core in the middle) in blast mitigation became a topology of choice as designers realized that a crushable core, which can dissipate a substantial amount of energy, could attenuate the impulse transmitted to the back-side face sheet and therefore protect it from catastrophic failure. Numerous metallic sandwich architectures have been extensively studied and were shown to outperform monolithic structures of equal areal mass (Xue and Hutchinson, 2003, 2004; Fleck and Deshpande, 2004; Qiu et al., 2004; Deshpande and Fleck, 2005; Hutchinson and Xue, 2005; Qiu et al., 2005; Liang et al., 2007; Mori et al., 2007, 2009; Vaziri et al., 2007;). Fleck and Deshpande (2004) suggested that the dynamic response of

* Corresponding author.
E-mail address: espinosa@northwestern.edu (H.D. Espinosa).
[1] Current affiliation: EDF–R&D, MMC, Avenue des Renardières, 77818 Moret-sur-Loing, France.

0022-5096/$ - see front matter
http://dx.doi.org/10.1016/j.jmps.2013.02.007

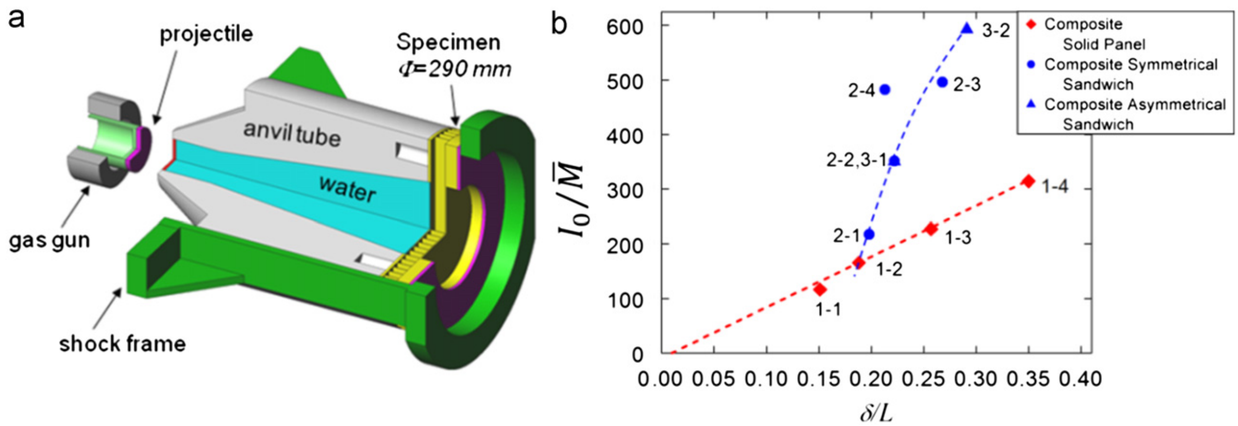

Fig. 1. (a) Schematic of the FSI experimental apparatus; (b) Impulse per areal mass vs. normalized deflection for monolithic, symmetrical, and asymmetrical sandwich composite panels reported in (Latourte et al., 2011).The notation represents "panel configuration – test number"; for example, test ♯ "1-1", "2-1" and "3-1" refer to test ♯1 on solid, symmetric, and asymmetric composite panels, respectively.

sandwich panels can be discretized into three stages: Stage I, fluid–structure interaction before first fluid cavitation; Stage II, core compression; Stage III, panel bending and stretching. Adopting Fleck and Deshpande's model, Hutchison and Xue (2005) studied the relationship between the ratio of the momentum transferred to the core and the back-side face sheet over the total imparted momentum and the compressive core crushing strength. Having shown better performance (i.e., higher energy absorbance per unit areal weight) than monolithic structures (Rathbun et al., 2006; Dharmasena et al., 2010), metallic sandwich structures still suffer from shortcomings. For example, the dramatic variation in the stiffness of a metallic core when subjected to buckling and followed by re-strengthening (fully collapsed core) makes optimized design of sandwich structures, over a wide range of applied impulses, very difficult (Hutchinson and Xue, 2005; Vaziri et al., 2006; Lee et al., 2006; McShane et al., 2010).

Recently, fiber reinforced polymer composite materials and cellular polymer foams have been utilized to replace metals in sandwich architectures. Because they have strength comparable to high strength steels, yet much lower material density, fiber reinforced composites are used as skin materials in composite ships (LeBlanc and Shukla 2011; Dear and Brown, 2003). Polymer foams are chosen as core materials because of their high energy absorption capabilities during compression (Andrews and Moussa, 2009; Tagarielli et al., 2010; Wang and Shukla, 2011; Gardner et al., 2011; LeBlanc and Shukla, 2011). Despite the large volume of literature on sandwich structures (Hoo Fatt and Palla, 2009; Abrate, 2005, 2011; Massabò and Cavicchi, 2011; Hoo Fatt and Surabhi, 2012; Arora et al., 2011, 2012; Dear et al., 2005), numerical studies of fluid–structure interaction (FSI) problems that occur when underwater blast is applied to these structures are limited.

In an earlier study (Latourte et al., 2011), we reported experiments on monolithic and sandwich composite panels subjected to a wide range of impulsive loading using a scaled-down FSI apparatus (Espinosa et al., 2006), as shown in Fig. 1a. Each composite lamina in the panels contained four unidirectional plies consisting of Devold DBLT850-E10 glass-fibers infiltrated by vinylester Reichhold DION 9500 resin aligned in a sequence of either ($0^\circ/45^\circ/90^\circ/-45^\circ$) or ($45^\circ/90^\circ/-45^\circ/0^\circ$). Four monolithic (solid) panels (panel configuration 1), four symmetric sandwich panels (panel configuration 2), and two asymmetric sandwich panels (panel configuration 3) were tested at impulses ranging from 1233 to 6672 Pa s. Postmortem characterization was also performed to identify different damage mechanisms, such as inter-lamina delamination, fiber and matrix damage in the composite plies, and foam crushing. The performances of the three types of panels were summarized by plotting the applied impulse per areal mass vs. the observed central deflection (Fig. 1b).

In this paper, we report models used to simulate the FSI experiments to assess their accuracy and predictive capabilities. We start by examining various approaches to simulate the FSI effect. Next we introduce the failure models used for the fibers and the matrix, a rate-dependent cohesive law to model inter-lamina delamination, and a foam crush model. We then present the model validation using test ♯1–3 (the 3rd monolithic composite panel) and a discussion of model predictions for both monolithic and sandwich panels over a wide range of impulses. We close with remarks on remaining issues and future work needs.

2. Numerical model

Three approaches have been widely used to simulate the fluid–structure interaction in air/water blast problems. The first approach is to simulate both the fluid media and solid structure with Lagrangian meshes (L-L model) (Espinosa et al., 2006). The fluid behavior is described with a Mie-Grüneisen equation of state (EOS) with a linear Hugoniot relation. An adaptive remeshing technique is required to prevent large distortion of the fluid mesh during wave propagation and interaction with the solid structures. However, remeshing cannot completely solve the element distortion problem at high impulses or when a large fluid cavitation occurs. Recently, a coupled Eulerian–Lagrangian technique (CEL or E–L model) has been used to simulate problems involving complex interactions between fluid and solid structures (Latourte et al., 2012). The fluid behavior is described with the same EOS as in the L-L model; however, using an Eulerian mesh in the fluid domain eliminates the element distortion problem. In addition, the variable “material volume fraction” in the integration points of the Eulerian mesh gives a direct measure of fluid cavitation formation and collapse. Using the E–L model, we successfully performed numerical simulations on the FSI experiments on high strength steels (Latourte et al., 2012). However, capturing the fluid front for the water in contact with the sample at the boundary of the pressurized region, required extending the Eulerian mesh beyond the original fluid domain, which usually results in difficulties achieving a fine Eulerian mesh density. Moreover, contact between the Eulerian surface and the Lagrangian surface artificially becomes too stiff when the coarse Eulerian mesh is used. For composite panels in which the moduli of each element is one to two orders of magnitude smaller than steel, an accurate contact description is the key to correctly capture unique damage mechanisms such as inter-lamina delamination. Thus, in this study, a third approach known as an acoustic and Lagrangian formulation (A-L model) was employed.

2.1. Acoustic fluid–structure interaction model

In the A-L model, the fluid body (a water column for this study) is modeled as an acoustic medium. The dynamic equilibrium equation for an acoustic medium is expressed as

$$\frac{\partial p}{\partial \boldsymbol{x}} + \gamma \dot{\boldsymbol{u}}^f + \rho_f \ddot{\boldsymbol{u}}^f = 0 \tag{1}$$

where p is the excess pressure in the fluid (static pressure), $\dot{\boldsymbol{u}}^f$ and $\ddot{\boldsymbol{u}}^f$ are the fluid particle velocity and acceleration, respectively, ρ_f is the fluid density, and γ is the volumetric drag coefficient (force per unit volume and velocity) (Abaqus 6.9-ef online documentation, 2009). With assumptions of inviscid, linear, and compressible fluid, the constitutive law for an acoustic medium is given as

$$p = -K_f \frac{\partial \boldsymbol{u}^f}{\partial \boldsymbol{x}} \tag{2}$$

where K_f is the bulk modulus of the fluid. In this study, a total of approximately three million eight-node linear acoustic brick elements with an average size of $1 \times 1 \times 1\ \text{mm}^3$ were used. The density and bulk modulus of water are $\rho_f = 985.27\ \text{kg/m}^3$ and $K_f = 2.19$ GPa, respectively. Because water cannot withstand significant tensile stress and is likely to form cavities under tensile pressure, a fluid cavitation limit of $p_c = 3270$ Pa, the saturation vapor pressure at room temperature, was used to simulate cavitation in water.

The interaction between the fluid and solid domains was realized by tying the solid structure surfaces (set as master surfaces) to the acoustic medium surfaces (set as slave surfaces). By introducing the tie constraints, displacement degrees of freedom were added to the fluid surface nodes. In total, three tie constraints were employed during each numerical simulation: the top surface of the piston with the bottom surface of the water column; the inner surface of the anvil tube with the side surface of the water column; and the front sheet surface (wet surface) of the composite panel with the top surface of the water column (Fig. 2).

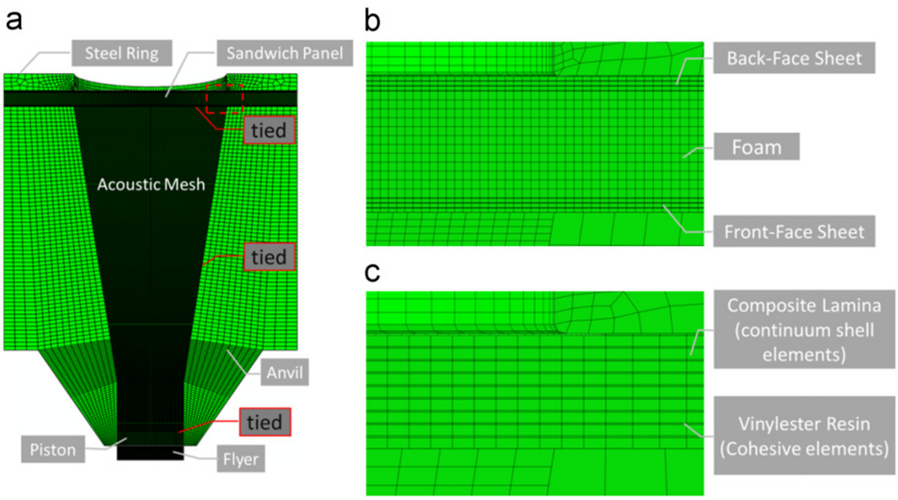

Fig. 2. Schematic of the FSI finite element model; (a) Cross-section view of the FSI experimental setup and the corresponding finite element mesh; (b) Magnified view of the sandwich panel mesh in the dashed square region in (a); (c) Magnified view of the solid panel mesh in the dashed square region in (a).

2.2. Unidirectional composite laminate degradation model (Hashin's model)

The composite laminas were modeled with eight-node quadrilateral in-plane continuum shell elements with an average size of $0.6\times0.8\times0.8\ \text{mm}^3$. A linear orthotropic elastic constitutive law was assigned on each of the four plies in individual laminas. Damage initiation and material failure of each unidirectional composite ply were investigated with Hashin's model (Hashin and Rotem, 1973; Hashin, 1980), which incorporates four material damage mechanisms: fiber damage in tension, fiber damage in compression, matrix damage in tension, and matrix damage in compression. With the x-axis along the fiber (longitudinal) direction and the y-axis along the transverse direction, the damage initiation equations in all four modes are:

Fiber tension ($\hat{\sigma}_{11}\geq 0$):

$$F_f^t=\left(\frac{\hat{\sigma}_{11}}{X^T}\right)^2+\alpha\left(\frac{\hat{\tau}_{12}}{S^L}\right)^2,\ \begin{cases} F_f^t<1 & \text{no damage}\\ else & \text{damage}\end{cases} \tag{3}$$

in which α determines the contribution of the shear stress to the fiber tensile damage initiation, which in this study was set to $\alpha=1$(Hashin, 1980);

Fiber compression ($\hat{\sigma}_{11}<0$):

$$F_f^c=\left(\frac{\hat{\sigma}_{11}}{X^C}\right)^2,\ \begin{cases} F_f^c<0 & \text{no damage}\\ else & \text{damage}\end{cases} \tag{4}$$

Matrix tension ($\hat{\sigma}_{22}\geq 0$):

$$F_m^t=\left(\frac{\hat{\sigma}_{22}}{Y^T}\right)^2+\left(\frac{\hat{\tau}_{12}}{S^L}\right)^2,\ \begin{cases} F_m^t<0 & \text{no damage}\\ else & \text{damage}\end{cases} \tag{5}$$

Matrix Compression ($\hat{\sigma}_{22}<0$):

$$F_m^c=\left(\frac{\hat{\sigma}_{22}}{2S^T}\right)^2+\left[\left(\frac{Y^C}{2S^T}\right)^2-1\right]\frac{\hat{\sigma}_{22}}{Y^C}+\left(\frac{\hat{\tau}_{12}}{S^L}\right)^2,\ \begin{cases} F_m^c<0 & \text{no damage}\\ else & \text{damage}\end{cases} \tag{6}$$

In Eqs. (3)–(6), X^T and X^C are the tensile and compressive strengths of unidirectional composite in the fiber direction, Y^T and Y^C are the tensile and compressive strengths in the matrix direction, and S^L and S^T are the longitudinal and transverse shear strengths. In addition, $\hat{\sigma}_{11}$, $\hat{\sigma}_{22}$, and $\hat{\tau}_{12}$ are the components of the effective stress tensor, $\hat{\boldsymbol{\sigma}}=M\boldsymbol{\sigma}$, in which σ is the nominal stress tensor and M is the damage operator (Lapczyk and Hurtado, 2007):

$$M=\begin{bmatrix}\frac{1}{(1-d_f)} & 0 & 0\\ 0 & \frac{1}{(1-d_m)} & 0\\ 0 & 0 & \frac{1}{(1-d_s)}\end{bmatrix}. \tag{7}$$

In Eq. (7), d_f, d_m, d_s are the damage variables in fiber, matrix, and shear mode:

$$d_f=\begin{cases} d_f^t,\ \text{fiber tensile damage variable, if } \hat{\sigma}_{11}\geq 0\\ d_f^c,\ \text{fibercompressive damage variable, if } \hat{\sigma}_{11}<0\end{cases}$$

$$d_m=\begin{cases} d_m^t,\ \text{matrix tensile damage variable, if } \hat{\sigma}_{22}\geq 0\\ d_m^c,\ \text{matrix compressive damage variable, if } \hat{\sigma}_{22}<0\end{cases}$$

$$d_s=1-(1-d_f^t)(1-d_f^c)(1-d_m^t)(1-d_m^c). \tag{8}$$

By inputting G_{ft}^C, G_{fc}^C, G_{mt}^C, and G_{mc}^C, which are the fracture toughness values in fiber tension and compression, and matrix tension and compression modes, and assuming a linear softening model during damage evolution, the five damage variables in Eq. (8) can be assessed. The material properties of unidirectional E-glass fiber-reinforced vinylester resin composites are listed in Table 1 and were independently identified or taken from the literature. To have full control of the progressive damage in various modes, we implemented Hashin's model with an user-defined subroutine, VUMAT, for ABAQUS/Explicit via an approach similar to that reported in (Lapczyk and Hurtado, 2007).

2.3. Strain-rate dependent cohesive law

Delamination is a prominent failure mode in laminated composite materials subjected to transverse loads. It can cause a significant reduction in the bending stiffness of a structure and its compressive load-carrying capacity. The FSI experimental studies reported in (Latourte et al., 2011) have shown extensive impact-induced interface delamination between composite laminates bonded together by vinylester adhesive layers. Such debonding behavior can be simulated by the cohesive zone model (CZM), which is based on concepts first discussed by Dugdale (1960) and Barenblatt (1983). In the aforementioned literature and in various models provided in ABAQUS, the cohesive laws are rate-independent;

Table 1
Material properties of E-glass/vinylester unidirectional composite lamina.

Material property	Value	Material property	Value
Density, ρ	1850 kg/m^3	X^T	1.2 GPa (Daniel et al., 1994)
E_{11}	39 GPa (Daniel et al., 1994)	X^T	620 MPa (Daniel et al., 1994)
E_{22}	11.5 GPa (Daniel et al., 1994)	Y^T	50 MPa (Daniel et al., 1994)
G_{12}	3.5 GPa (Daniel et al., 1994)	Y^T	128 MPa (Daniel et al., 1994)
G_{13}	3 GPa (Daniel et al., 1994)	S^L	89 MPa (Daniel et al., 1994)
G_{23}	3 GPa (Daniel et al., 1994)	S^T	60 MPa (Daniel et al., 1994)
Poisson's ratio, ν	0.28 (Daniel et al., 1994)	$G_{ft}^C = G_{fc}^C$	35×10^3 N/m (Roy et al., 2001)
		$G_{mt}^C = G_{mc}^C$	2×10^3 N/m (Compston et al., 1998)

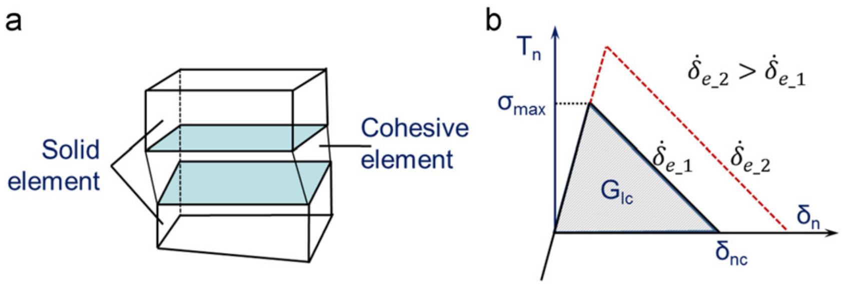

Fig. 3. (a) 3D eight-node cohesive element; (b) Rate-dependent bilinear cohesive model.

namely, the tractions within the cohesive zone depend only on the crack surface opening displacement and are independent of the crack opening rate. Dynamic compressive tests on pure vinylester resin (the matrix and interface material in this study), however, showed that its mechanical properties are highly sensitive to the loading rate (Oguni and Ravichandran, 2001). The strength of vinylester rises from 80 MPa in quasi-static compression to 200 MPa at a strain rate on the order of $1 \times 10^3\ \mathrm{s}^{-1}$. In the FSI tests presented here, the strain rate of the interface material can reach $50 \times 10^3\ \mathrm{s}^{-1}$ due to the fluid cavitation formation and collapse. Therefore, to accurately describe the inter-lamina delamination in composites, the strain rate must be included in the model. Several rate-dependent models have previously been introduced (Glennie, 1971; Xu et al., 1991; Tvergaard and Hutchinson, 1996; Costanzo and Walton, 1997; Samudrala et al., 2002; Espinosa and Zavattieri, 2003). A rate-dependent CZM was first introduced by Glennie (1971), where the traction in the cohesive zone is a function of the crack opening displacement time derivative. Xu et al. (1991) extended this model by adding a linearly decaying damage law. In each model, the viscosity parameter η is used to vary the degree of rate dependence.

Our approach employs a rate-dependent bilinear cohesive model, as illustrated in Fig. 3b, for the mode I failure process. The cohesive elements with finite thickness connect two volumetric elements with traction-separation laws (Fig. 3a) that relate the cohesive traction vectors $\mathbf{T}=\{T_n,T_{s1},T_{s2}\}2$ and the displacement jump vector $\boldsymbol{\delta}=\{\delta_n,\delta_{s1},\delta_{s2}\}$. Subscripts n and s denote the normal and tangential components, respectively. We adopted a simple bilinear cohesive law similar to that used in Espinosa and Zavattieri (2003) and Geubelle and Baylor (1998), namely,

$$T_n = \frac{D}{1-D}\frac{\sigma_{\max}}{D_{\text{initial}}}\frac{\delta_n}{\delta_{nc}}, \tag{9}$$

where $\sigma_{\max}$ and δ_{nc} denote the local values of the tensile failure strength and critical crack opening displacement of the material, respectively. Similar cohesive laws are applied for the traction and separation in shear directions. The damage parameter D is defined by

$$D = \left\langle 1-\sqrt{\left(\frac{\delta_n}{\delta_{nc}}\right)^2+\left(\frac{\delta_{s1}}{\delta_{sc}}\right)^2+\left(\frac{\delta_{s2}}{\delta_{sc}}\right)^2}\right\rangle, \tag{10}$$

where $\langle z\rangle = z$ for $z>0$ and $\langle z\rangle = 0$ otherwise. To prevent healing of the cohesive zone in the event of unloading, D was constrained to monotonic decrease from its initial value D_{initial}, typically chosen close to unity, to its final value of zero, at which point complete failure is reached. The area under the cohesive failure curve corresponds to the mode I fracture toughness G_{Ic}, which is given by

$$G_{Ic} = \frac{1}{2}\delta_{nc}\sigma_{\max}. \tag{11}$$

This formulation is fully three dimensional and can simulate mixed-mode delamination. To account for rate dependence in the cohesive law, we adopt the rate-dependent cohesive law proposed by Espinosa and Zavattieri (2003) in which the interfacial strengths and critical displacement jumps are related to the opening rate of cohesive surfaces, namely,

$$\sigma_{\max} = \sigma_{\max}^{ref} \cdot \left(1+\eta \ln\left(\frac{\dot{\delta}_e}{\dot{\delta}_e^{ref}}\right)\right)$$
$$\delta_c = \delta_c^{ref} \cdot \left(1+\eta \ln\left(\frac{\dot{\delta}_e}{\dot{\delta}_e^{ref}}\right)\right), \tag{12}$$

where $\dot{\delta}_e^{ref}$, $\sigma_{\max}^{ref}$, δ_c^{ref}, and η are the reference effective displacement jump rate, initial cohesive strength, initial critical displacement jump, and rate sensitivity parameter, respectively. The effective displacement jump in each cohesive element is calculated as

$$\delta_e = \sqrt{\delta_n^2+\delta_{s1}^2+\delta_{s2}^2}. \tag{13}$$

The rate-dependent cohesive model was formulated and implemented in ABAQUS/explicit 6.9 EF (2009) through a user-defined element subroutine (VUEL). In the current model, the reference strain rate for vinylester is set to $\dot{\delta}_e^{ref} = 1\ \mathrm{ms}^{-1}$, the reference strength is set to $\sigma_{\max}^{ref} = 80$ MPa, and the reference fracture toughness values in mode I and II are both set to $G_{Ic}^{ref} = G_{IIc}^{ref} = 1\times10^3\ \mathrm{J\,m}^{-2}$ (Compston et al., 1998; Oguni and Ravichandran, 2001).

2.4. Crushable foam plasticity model with volumetric hardening and strain rate dependence

The foam core used in the composite sandwich panels is Divinycell H250 PVC foam, with a density of 250 kg/m^3. The quasi-static and dynamic compressive properties of H250 foam have been well studied by Deshpande and Fleck (2001), Tagarielli et al. (2008). The foam constitutive behavior is described by the crushable foam plasticity model first developed by Deshpande and Fleck (2000). This model, which includes volumetric hardening, uses a yield surface defined as

$$F = \sqrt{q^2+\beta^2(p-p_0)} - B = 0, \tag{14}$$

where p is the pressure stress, q is the von Mises stress, and $\beta = B/A$ is the shape factor of the yield surface. A is the size of the yield ellipse along the p-axis, and B is the size of the yield ellipse along the q-axis. Furthermore, the shape factor can be expressed as

$$\beta = \frac{3k}{\sqrt{(3k_t+k)(3-k)}}, \text{ with } k = \frac{\sigma_c^0}{p_c^0} \text{ and } k_t = \frac{p_t}{p_c^0}, \tag{15}$$

where σ_c^0 is the initial yield stress in uniaxial compression, p_c^0 is the initial yield stress in hydrostatic compression, and p_t is the yield strength in hydrostatic tension. Fitting the experimental data on the H250 PVC foam reported in (Deshpande and Fleck, 2001; Tagarielli et al., 2008) with the yield surface function given by Eq.(14) yields $k = k_t = 1.5625$. The evolution of the yield surface is realized by inputting the uniaxial compressive stress–strain response of the foam, using data adapted from the study by Tagarielli et al. (2008).

Because the FSI experiments involve deformations at high strain rates (up to $10^3\ \mathrm{s}^{-1}$), the strain rate effect has to be incorporated in the numerical model. In Tagarielli et al. (2008), the yield strength of the H250 PVC foam was found to be highly sensitive to the compressive strain rate. Fitting the dynamic experimental data, they reported a power law relation

$$\frac{\sigma_y}{\sigma_y^0} = \left(\frac{\dot{\varepsilon}}{\dot{\varepsilon}_0}\right)^m \tag{16}$$

with the reference strain rate $\dot{\varepsilon}_0 = 1\ \mathrm{s}^{-1}$, the reference yield stress $\sigma_y^0 = 7.44$ MPa, and the power law exponent $m = 0.048$.

Given an elastic modulus of 170 MPa, a Poisson's ratio of 0.3, and the plastic properties identified above, the foam core was modeled by approximately 0.75 million eight-node linear brick elements with an average mesh size of $0.8\times0.8\times1.25\ \mathrm{mm}^3$.

2.5. Projectile, piston, and other components

The projectiles and pistons in this study were made of heat treated AISI 4140 steel, the anvil tube was made of wrought 4340 steel, and the steel rings to clamp the panels were made of AISI 1018 steel (Fig. 2). The material properties of all the steels used are listed in Table 2. All steel components were modeled with eight-node linear brick elements. The mesh size of the projectiles and pistons was approximately $1\times1\times1\ \mathrm{mm}^3$. The anvil tube and steel clamp had an average mesh size of $2\times2\times2\ \mathrm{mm}^3$ where contact interactions were defined. Between the steel clamp and panel, a thin resin layer (with an

Table 2
Material properties of the steels used in the FSI model.

Material	AISI 4140 steel	Wrought 4340 steel	AISI 1018 steel
Density	7850 kg/m^3	7850 kg/m^3	7850 kg/m^3
Young's modulus	205 GPa	205 GPa	205 GPa
Poisson's ratio	0.29	0.29	0.3
Yield strength	675 MPa	470 MPa	205 MPa
Strain hardening exp.	0.09	–	–

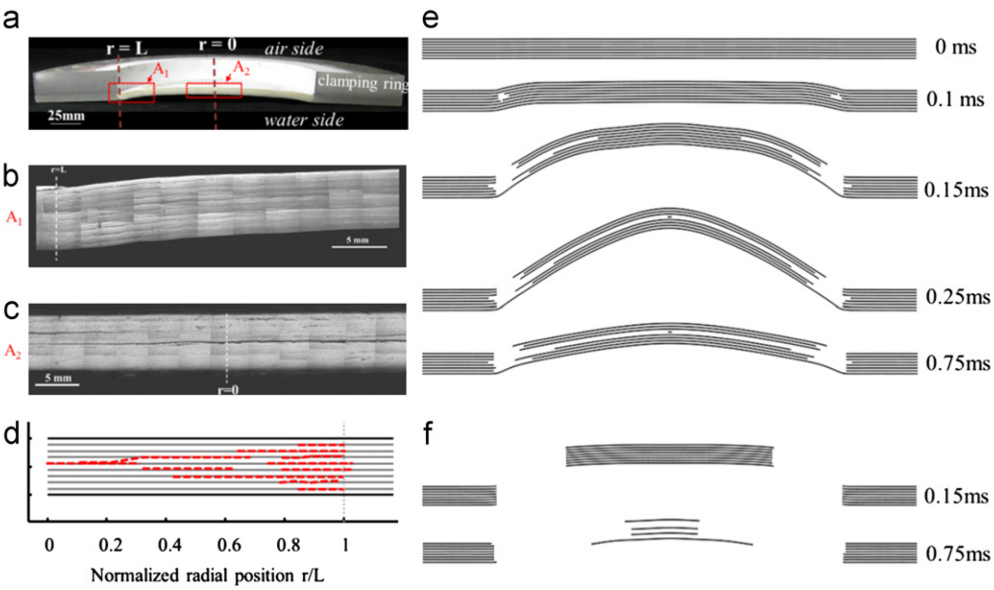

Fig. 4. (a) Cross-section view of the monolithic panel ♯1-3 after the test; (b) and (c) Optical micrographs of inter-lamina delamination close to the clamped edge (region A_1 in (a)) and at the center (region A_2 in (a)), respectively; (d) Schematic of the interface delamination pattern along the radial position; Predicted interface delamination history with a strain-rate sensitive cohesive law (e), and with a rate-independent cohesive law (f).

average mesh size of $1 \times 1 \times 0.1$ mm^3) was created to introduce the bonding condition using tie constraints. Clamping of the sample was realized by introducing a fixed displacement boundary condition on the top of the steel clamp.

3. Numerical results and discussion

3.1. Strain-rate sensitive cohesive law and composite model calibration

With the material properties listed in Section 2, the remaining task was to assess the strain-rate sensitivity of the vinylester resin, which was calibrated by comparing the inter-lamina delamination patterns from simulations with those observed in experiments. In this study, test ♯1-3 (at an impulse of 2425 Pa s) was chosen as the control experiment to calibrate the strain-rate sensitivity cohesive model because it gives a complex delamination pattern with no catastrophic fiber rupture. A parametric study was performed to determine the effect of the strain-rate sensitivity coefficient η on the delamination pattern. By comparing the interface failure distribution in the simulation with that observed in the test, we found that $\eta = 0.25$ yields the best correlation with the experimentally measured delamination patterns (Latourte et al., 2011). As shown in Fig. 4a, micrographs of the cross-section reveal characteristic delamination patterns in the monolithic composite panel (test ♯1-3). At the clamped edge, delamination at all eight interfaces developed due to shearing, with partial propagation to the center of the panel (Fig. 4b). As deformation of the panel increases, a delamination front propagates along the central interface (Fig. 4c). The simulated delamination history is shown in Fig. 4e. Delamination initiates at the clamped boundaries and propagates toward the center. Both the panel deflection and delamination reach their maximum at approximately 0.25 ms. Then, a spring back of the panel is observed and no further delamination is predicted. The final delamination pattern agrees well with that observed in the experiment (Fig. 4a–d). When delamination-rate effects are turned off, the predicted delamination history is very different and more extensive interface failure is present in the simulation than is observed in the experiment (Fig. 4f).

Numerical predictions of the central deflection history (with and without a rate-dependent cohesive law), together with the experimental measurement, are plotted in Fig. 5. Interestingly, no major difference is found between the two simulations with both following the recorded center panel deflection reasonably well. For the rate-dependent cohesive law, a maximum deflection of about 19.8 mm and a final deflection of about 7.2 mm are predicted, which compare favorably with the experimentally measured values of 19.5 mm and 6.7 mm. The simulation result using a rate-independent cohesive law shows an almost constant deflection rate and yields a small overshoot in maximum deflection. The deflection profiles across the panel at various instants in time are compared with those measured by means of shadow Moiré (Latourte et al., 2011), as shown in Fig. 6. Again, the simulated deformations in the bulging and spring-back regimes agree well with the experimental profiles.

Fiber and matrix damage patterns have also been extracted from the simulation results. As shown in Fig. 7a, the fibers on the water-side and air-side laminates begin to show damage at the clamped edge and outer region, respectively. However, the panel shows no evidence of catastrophic failure. Meanwhile, the matrices in both laminates show more

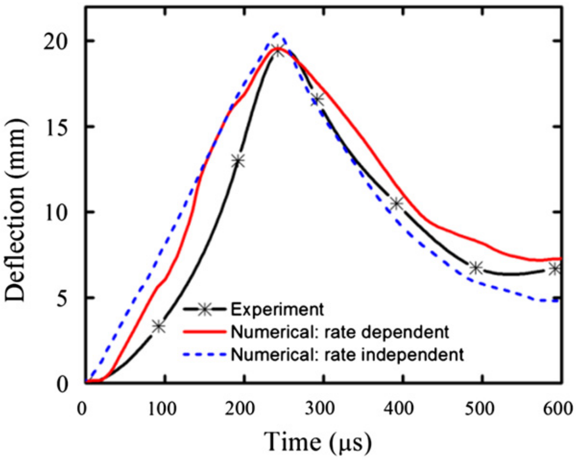

Fig. 5. Experimental central deflection history compared with those from numerical simulations. The solid line corresponds to the model with a rate-dependent cohesive law while the dashed line corresponds to the model with a rate-independent cohesive law.

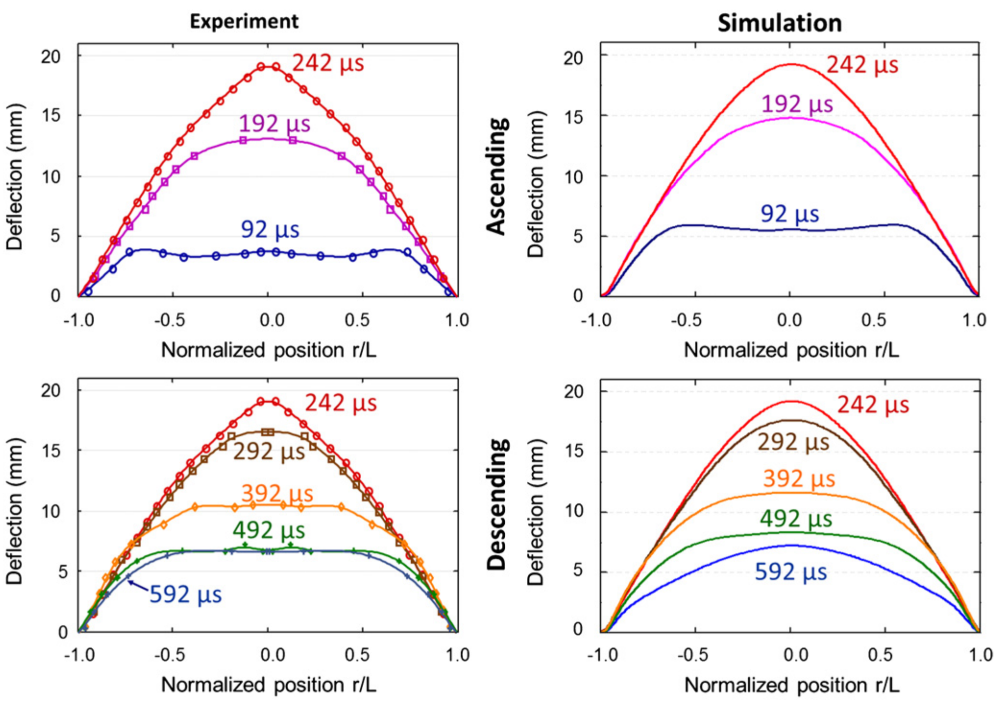

Fig. 6. Ascending and decending deformation histories across panel ♯1-3 as obtained from experimental measurements (left) and simulation results (right).

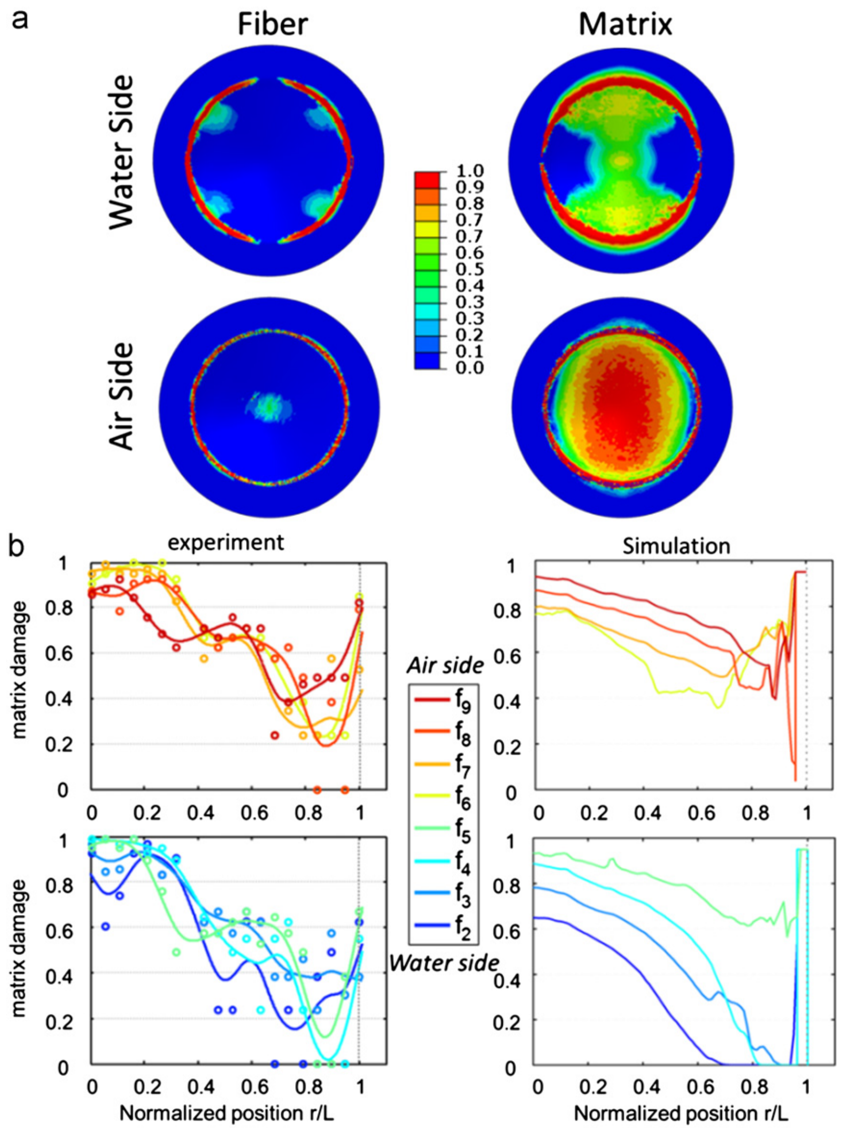

Fig. 7. (a) Fiber and matrix damage patterns in the water-side and air-side laminas for test ♯1-3 where the damage variable from 0 to 1 represents the damage level from low to high; (b) Comparison of matrix damage variables in individual lamina as a function of panel radial position from experiments and simulations for test ♯1-3. In this plot, $f_i(i=1,2,\ldots,9)$) represents the laminas from the water-side to the air-side (the result for f_1 was not given in (Latourte et al., 2011) due to extensive noise and uncertainties in the measurements).

severe and anisotropic damage patterns. The matrix damage d_m along the radius was extracted from the simulation and compared with the experimentally measured results (Latourte et al., 2011) (Fig. 7b). We found that the experiment and simulation follow a similar trend – the matrix damage is maximized at the center due to high bi-axial tension, which becomes more pronounced when the water cavity collapses due to the FSI effect. The matrix damage is reduced toward the clamped edge but is still present due to bending effects. Overall, the model predicted a higher matrix damage level than was measured experimentally at the clamped boundaries for some water-side laminas. This is likely due to the fact that a rate-independent laminate model was employed. It is known that the strength and toughness of the matrix material in composites tends to increase with strain rates (Hsiao and Daniel, 1998; Hsiao et al., 1999; Daniel et al., 2011). To further demonstrate the capability of the FSI model in describing the interaction between the water column and the panel, a video clip of the simulation result of test ♯1-3 is provided (see Video 1, available online). In particular, the video shows that the rate-dependent cohesive law accurately captures the evolution of interlaminate debonding throughout the test.

Supplementary material related to this article can be found online at http://dx.doi.org/10.1016/j.jmps.2013.02.007.

Given the very good agreement between numerical and experimental results for test ♯1-3 concerning interface delamination, panel deformation, and fiber and matrix damage patterns, the calibrated finite element FSI model was next used to predict panel deformation and damage patterns in both monolithic and sandwich composite panels as a function of applied impulse. The implementation of the model in monolithic and sandwich composite panels at various impulse levels is discussed in Section 3.2.

3.2. Model predictions on monolithic panels

We began by examining the center deflection history and delamination pattern in test ♯1-1, which was subjected to a low impulse of 1233 Pa s. The central deflection history from the simulation was compared with that measured in the experiment (Fig. 8). Overall, the simulation agrees favorably with the experiment, although the simulation shows features that are not present in the experimental record. Note that the combination of shadow Moiré and high-speed photography provides only a limited number of points, rather than a continuous record. The largest observable discrepancy is in the spring-back phase where the simulation predicts a larger initial spring back with greater oscillations.

The simulation predicts that the inter-lamina delamination evolution occurs as one major inter-lamina crack that extends through the panel and stops at the constrained boundary, which agrees well with the experimental observation (Fig. 9a and b). Furthermore, the numerical model predicts delamination segments that initiate around the center region of

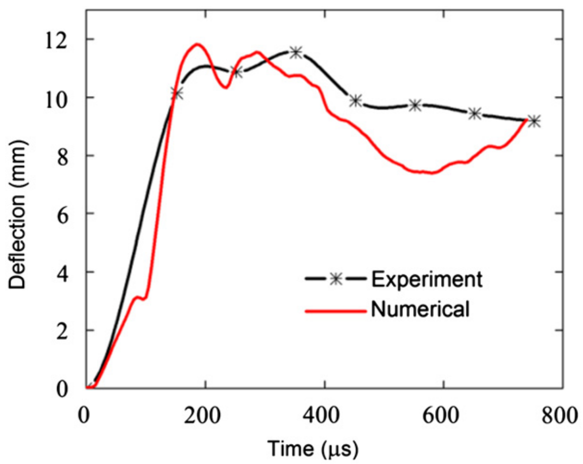

Fig. 8. Comparison between the central deflection histories obtained from experiment and numerical simulation for test ♯1-1.

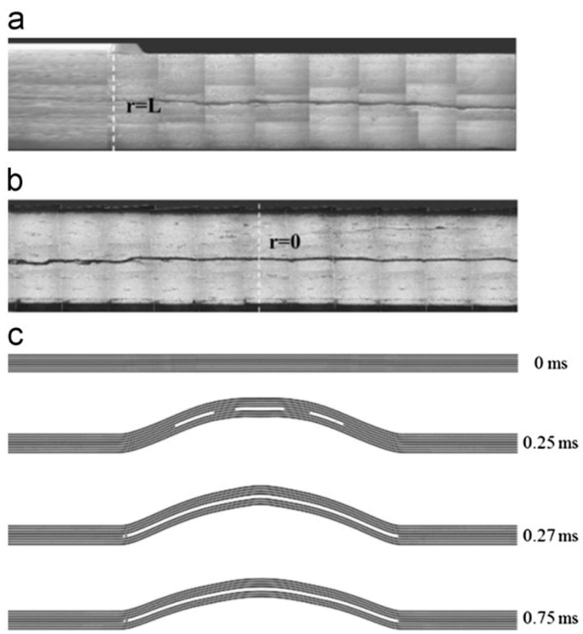

Fig. 9. (a) and (b) Micrographs of inter-lamina delamination patterns at the clamped boundary and around the center of the panel, respectively; (c) The interface delamination evolution predicted by the numerical model.

the panel, coalesce with each other, and then propagate toward the clamped edges (Fig. 9c). In contrast, test ♯1-3, which was subjected to an impulse almost twice as large, exhibited delamination initiation at the boundary with propagation toward the center of the panel.

Tests ♯1-2 (subjected to an impulse of 1766 Pa s) and ♯1-4 (subjected to an impulse of 3283 Pa s) were also simulated. The numerical model effectively describes the deflection rates in the bulging phase and the maximum center deflection of the panel (see Fig. 10). In test ♯1-2, the spring-back rate predicted in the simulation is smaller than that measured experimentally, but the residual deflection is captured accurately. In test ♯1-4, the simulation stops after 250 μs because of massive fiber failure and matrix damage. The end of the simulation coincides with the end of the experimental recording due to the loss of fringes in the shadow Moiré setup that result from such failure (Latourte et al., 2011).

3.3. Model prediction on sandwich panels

Being able to predict performance and damage in sandwich panels at different strain rates is of great interest due to their high performance toward blast loading and complex deformation mechanisms (Hutchinson and Xue, 2005). With a soft core added between panels, the effects of impulses to the front- and back-side face sheets are highly dependent on the material properties of the core, which can absorb a significant portion of the initial energy imparted. In addition, a sandwich panel has much greater bending strength than its monolithic counterpart because of the thick core added between the two face sheets. Among the six sandwich composite panels tested in (Latourte et al., 2011) (four symmetrical and two asymmetrical), test ♯2-3 is of the greatest interest due to the complexity of the observed failure mechanisms, which included foam crushing, initiation of fiber rupture failure, inter-lamina delamination, and signs of shear off at the clamped boundary. Fig. 11a shows plots of the central deflection of the back-side face sheet vs. the time predicted by the numerical model and measured in the experiment. In addition, the deformation history of the foam core is represented by plotting contours of the Lagrangian normal strain in the panel thickness direction (Fig. 11b). This illustrates the unique

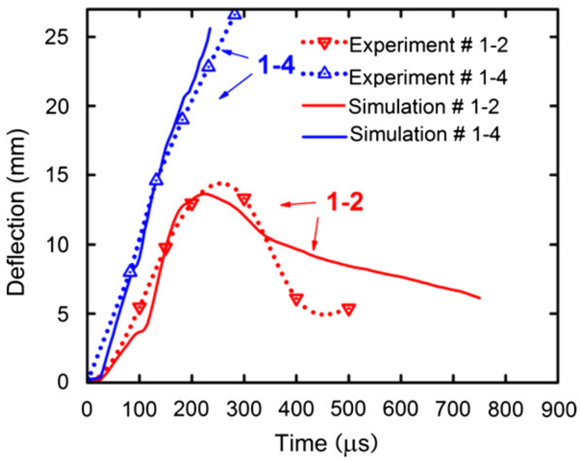

Fig. 10. Comparison between the central deflection histories from experiments (dash lines) and numerical simulations (solid lines) for monolithic panels in tests ♯1-2 and ♯1-4.

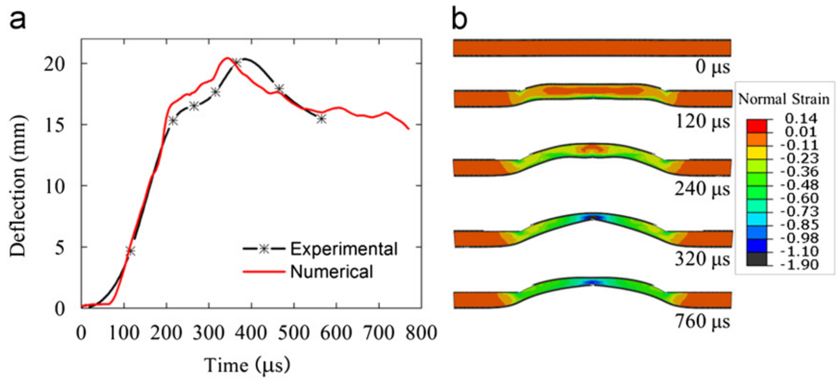

Fig. 11. (a) Comparison between the central deflection histories measured experimentally and predicted by numerical simulation for sandwich composite panel 2–3 at an impulse I_0 = 5581 Pa s; (b) Simulated deformation of the foam core represented as contour plots of Lagrangian normal strain in the panel thickness direction.

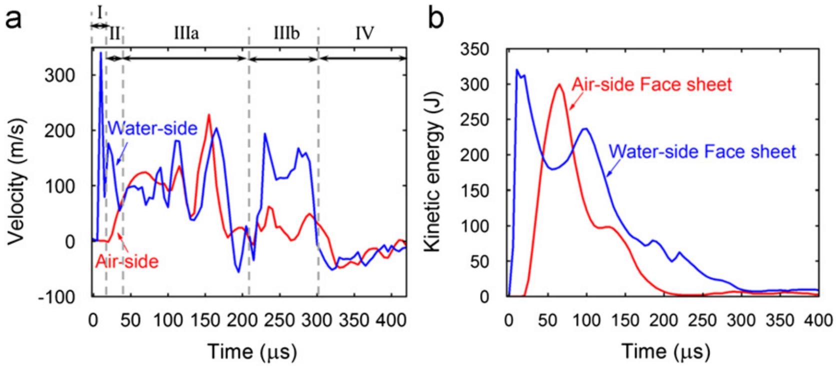

Fig. 12. (a) Plots of center-point velocity for the water-side and air-side face-sheets vs. time; (b) Plots of kinetic energy of the waterside and airside face sheets vs. time.

energy dissipation mechanism of foam core crushing that is present in sandwich panels. From 0 to 220 μs, the center of the panel moves at a nearly constant rate where an initial interaction between the water and the panel leads to water cavitation. At 220 μs, the cavity starts closing and the foam core begins to crush and absorb a large portion of the energy. The central deflection of the back-side face sheet (air side) slows down while that of the front face sheet (water side) accelerates. At approximately 320 μs, the cavitation collapse is complete and the foam is densified such that the front and back-side face sheets are displaced to the maximum deflection amplitude. After 320 μs, the panel springs back with a deflection recovery of about 5 mm. The numerical simulation correctly captures the panel deformation at each stage and correlates well with the experimental measurement.

The center point velocity histories of the front (water side) and back (air side) face sheets (Fig. 12a) reveal slightly more complex deformation phases than those proposed by Fleck and Deshpande (2004). The results are described by the following four stages:

- Stage I – initial fluid–structure interaction phase, from 0 to 20 μs, when the panel behaves similarly to a free-standing plate. In this phase, the water impulse impinges on the water-side face sheet and crushes a thin layer of the foam core behind it. Meanwhile, the air-side face sheet remains static. At the end of this phase, water cavitation begins.
- Stage II: core compression, from 20 to 40 μs, when the wave transmits through the whole panel and accelerates the air-side face sheet.
- Stage IIIa: panel bending and stretching, from 40 to 220 μs, when the air-side face sheet moves at a velocity similar to that of the water-side face sheet with lateral waves traveling across the panel.
- Stage IIIb: collapse of cavitated region, from 220 to 300 μs, when the water buble collapses and the foam core is crushed. A large amount of energy is dissipated during this phase.
- Stage IV: panel bending and stretching "recovery" phase, after 300 μs. During this phase, the foam, front- and back-side face sheets behave similar to a solid plate. Spring-back of the panel is observed.

Plots of the kinetic energy of the front- and back-face sheets as a function of time are shown in Fig. 12b and show that foam crushing mitigates the impulse transmitted to the back-face sheet. The duration of the impulse imparted on the back-face sheet is also shorter than the front-face sheet. In the front-face sheet, the kinetic energy has a second peak at around 110 μs; in contrast, the change in kinetic energy in the back-face sheet is much smoother and only has a small shoulder at approximately 140 μs.

Examination of damage along the panel cross section provides valuable insight. A cross-sectional view of sandwich panel 2–3 after the test is shown in Fig. 13a together with the deformed panel predicted by the simulation. Contours of Lagrangian normal strain (in the panel thickness direction) in the foam are also reported. Zooming in, the center region of the panel (region C_1 in Fig. 13a) shows significant foam crushing and two cracks in the foam extending from the water side at an $\sim 45^{\circ}$ angle from the face sheet surface (left panel in Fig. 13b). Under the foam, the water-side face sheet presents extensive delamination, matrix crushing, and fiber failure due to the impulse induced by water cavitation collapse. The model successfully captures these features (right panel in Fig. 13b). The center region of the foam undergoes a highly localized compressive strain up to -1.9. Although foam cracking is not accounted for in the model, a V-shaped normal strain concentration pattern is found, which suggests that the foam fails along the paths where shearing is maximized during compression. Inspecting the air-side face sheet near the clamped boundaries, inter-lamina delamination failure due to bending is found in both experiment and simulation results (Fig. 13c). In addition, another important failure mechanism is identified: shear off at the boundaries. As shown in Fig. 13d, one side of the sandwich panel at the clamped region exhibits failure in the foam beginning on the water-side face sheet. The crack initiated from the bottom and propagated almost vertically up to the air-side face sheet. This is a typical shear-off failure feature, which is a relevant failure mode in sandwich panels as suggested by Hutchinson and Xue (2005). Furthermore, they found that if shear off occurs, it does so

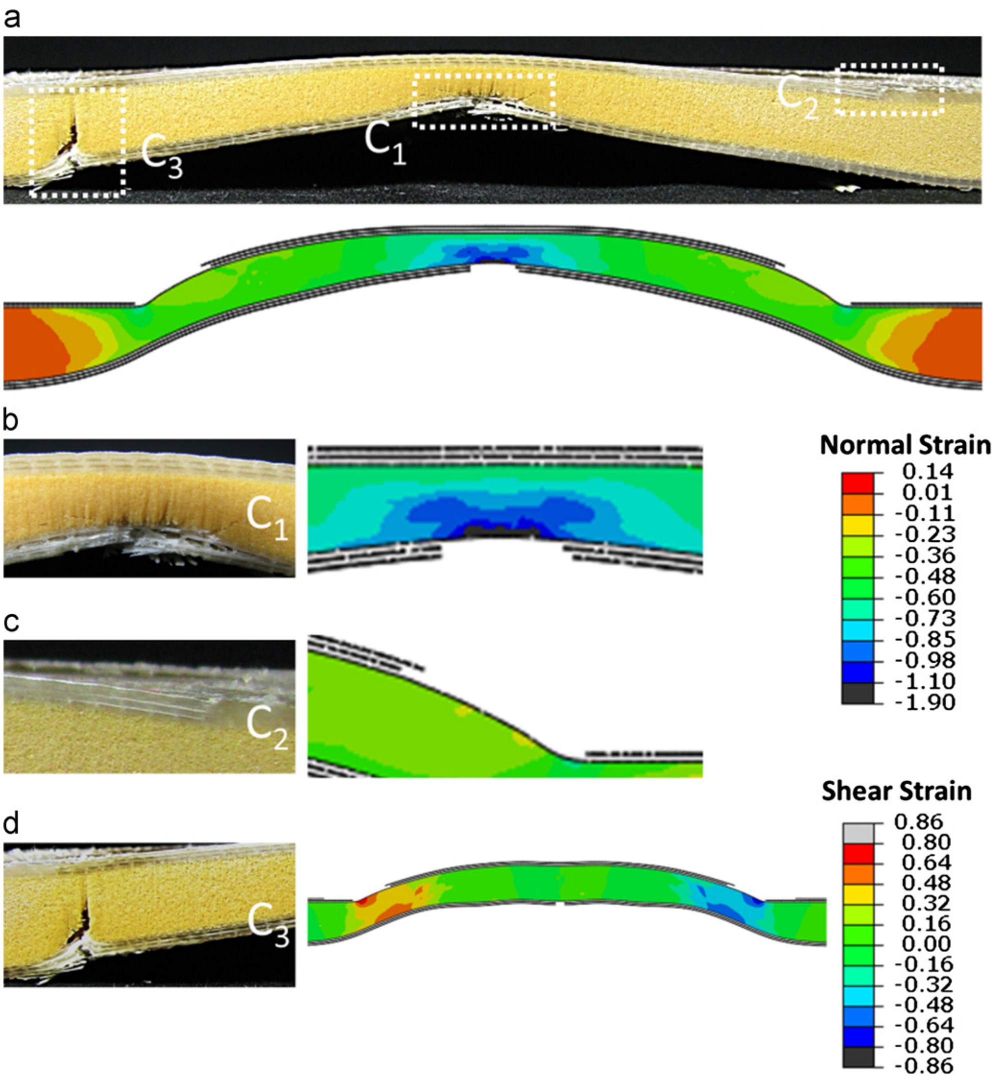

Fig. 13. (a) Cross-sectional views of sandwich panel 2–3 from the experiment (top) and numerical simulation (bottom) with contour plots of the Lagrangian normal strain in the foam in the panel thickness direction; (b) Magnified view of the sandwich panel center (region C_1 in panel (a)) in both the experiment and simulation (the Lagrangian normal strain in the foam is included); (c) Magnified view of the back-side face sheet around the clamped edge (region C_2) in both the experiment and simulation (the Lagrangian normal strain in the foam is included); (d) Magnified view of the shear off of the front face sheet around the clamped edge (region C_3) with the snap-shot of the sandwich panel deformation at 180 μs (the Lagrangian transverse shear strain in the foam is included).

very early in the history of the panel response prior to core crush and overall bending and stretching. This is also observed in the present simulation, as is evident from the Lagrangian shear strain contour plot at 180 μs after impact, just before major foam core crushing in the boundary.

Finally for panel 2–3, the fiber and matrix damage patterns predicted by the model are shown in Figs. 14a and 15b, respectively. Fiber tensile failure is significant along the fiber direction in both the water-side and air-side face sheets. Furthermore, an X-shaped failure pattern is found for both fiber and matrix damage modes in the water-side face sheet, which suggests that the fiber failure initiates along the regions where shear damage is maximized (Fig. 14b). In Hashin's model, the fiber tensile damage is assured to be enhanced by the in-plane shear stress (Eq. (3) when α is set to 1). When the matrix fails in shear, stress concentrations in the fibers develop and eventually cause their rupture. A photograph of the water-side face sheet (Fig. 14c) shows an X-shaped fiber failure region in agreement with the model prediction. A minor difference between the simulation and experimental results is that the fiber completely failed in the X-shaped pattern near the center in the experiment whereas the fiber damage level predicted by the model is approximately 60%.

Another numerical simulation was performed on panel 2–1, which was tested under a low impulse of $I_0 = 2465$ Pa s. The maximum deflection predicted by the model is approximately 15.8 mm, which is very similar to the experimental value of 15.2 mm. Plotting the velocity of the center points on the water-side and air-side face sheets yields no significant

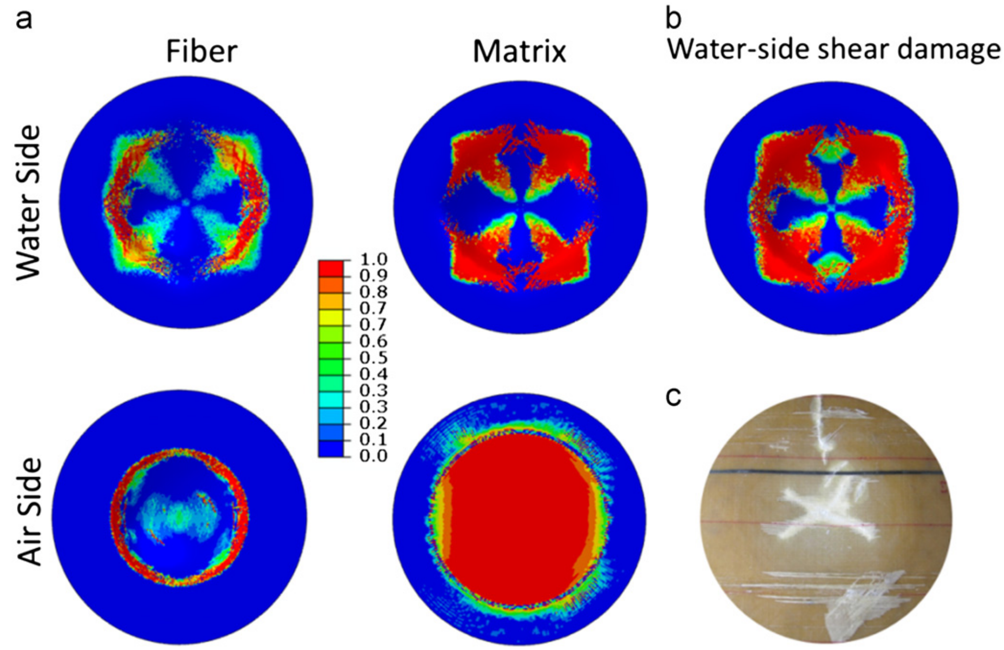

Fig. 14. (a) Fiber and matrix damage patterns in the water-side and air-side face sheets (damage variable from 0 to 1 represents the damage level from low to high); (b) Shear damage pattern, d_s in Eq. (8), in the water-side face sheet; (c) Photograph of the fiber failure pattern in the water-side face sheet of sandwich panel 2–3.

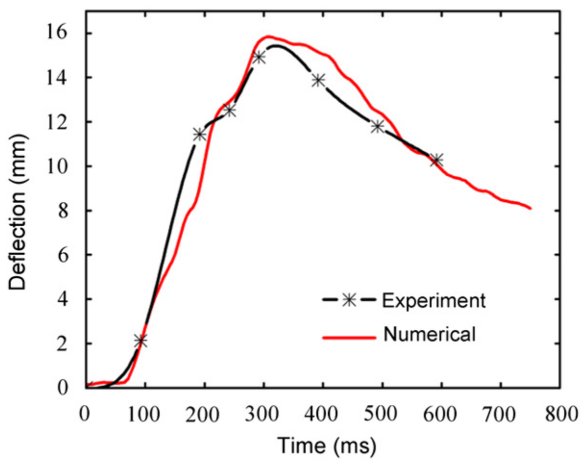

Fig. 15. Plots of panel central deflection vs. times measured experimentally and predicted by numerical simulation for sandwich panel 2–1 at an impulse $I_0 = 2465$ Pa s.

differences (Fig. 16a) with the exception of the first 20 μs. This prediction suggests a more limited water cavitation and less associated foam crushing. After 150 μs, the two skins and core move almost synchronously with no observable secondary foam-crushing event or cavitation collapse. As shown in Fig. 16c, in general, the foam core has an average normal compressive Lagrangian strain of -0.15 with only the boundary layers reaching a compressive strain of -0.6. This agrees well with the experimental observations (Fig. 16d).

Interestingly, the simulation results give a much higher ratio of peak kinetic energy of the back-side face sheet to the front-side face sheet, in comparison with test ♯2-3. Moreover, the kinetic energies of both skins exhibit significant oscillation, especially for the kinetic energy of the air-side face sheet with a major peak at 175 μs. All of these features suggest that the impulses imparted on both skins are not uniform, which in turn affect the damage distribution in each component.

Investigating the fiber and matrix failure patterns in the water-side and air-side face sheets in test ♯2-1 provides interesting information that aids our understanding of deformation and materials damage in sandwich composite structures. As shown in Fig. 17, test ♯2-1 shows much less fiber failure compared with test ♯2-3 (Fig. 14). In the water-side

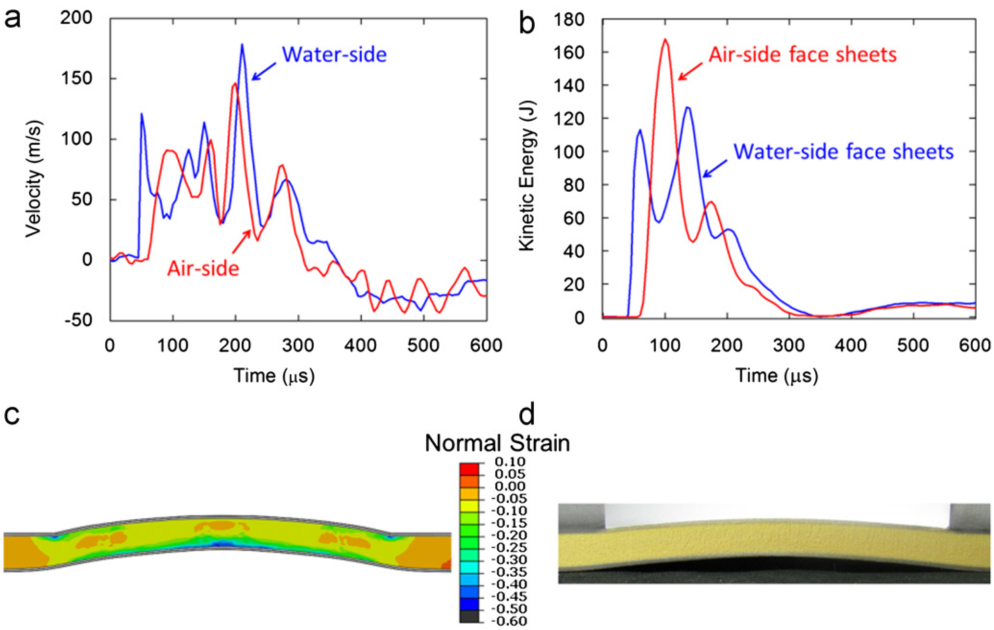

Fig. 16. (a) Central point velocities vs. time for the water-side and air-side face sheets predicted by the model for test ♯2-1; (b) Kinetic energies vs. time for the water-side and air-side face sheets predicted by the model for test ♯2-1; (c) Model predicted deformation of panel 2–1 with the contour plot of Lagrangian normal strain (in the panel thickness direction) in the foam; (d) Cross-sectional view of panel 2–1 after the test, showing no appreciable crushing of the foam.

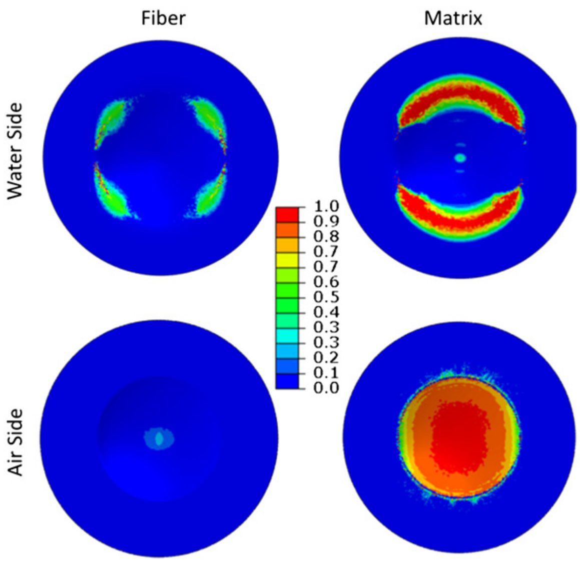

Fig. 17. Numerically predicted fiber and matrix damage patterns on the water-side and air-side face sheets for test ♯2-1 (damage variable from 0 to1 represents the damage level from low to high).

face sheet, the matrix damage is concentrated around the clamped boundaries, probably due to shear and bending. In the air-side face sheet, massive matrix damage is found in the center region, indicating the matrix fails from a more uniformly distributed tension of the foam core.

The unique damage patterns in sandwich composite panels are directly related to the foam core. The soft core dissipates a large portion of energy. In addition, core crushing significantly affects the ratio between impulses imparted on the front-side and back-side face sheets. Therefore, it is interesting to compare the energy dissipated in three regions in tests ♯2-1 and ♯2-3. At the low impulse (test ♯2-1), the total energy is mainly dissipated by the core. A small portion of the energy is dissipated in the composite laminates (Fig. 18a). The percentages of energy dissipated are approximately 2.8%, 10.8%, and 86.4% for the water-side face sheet, air-side face sheet, and core, respectively. At high impulse (test ♯2-3), a

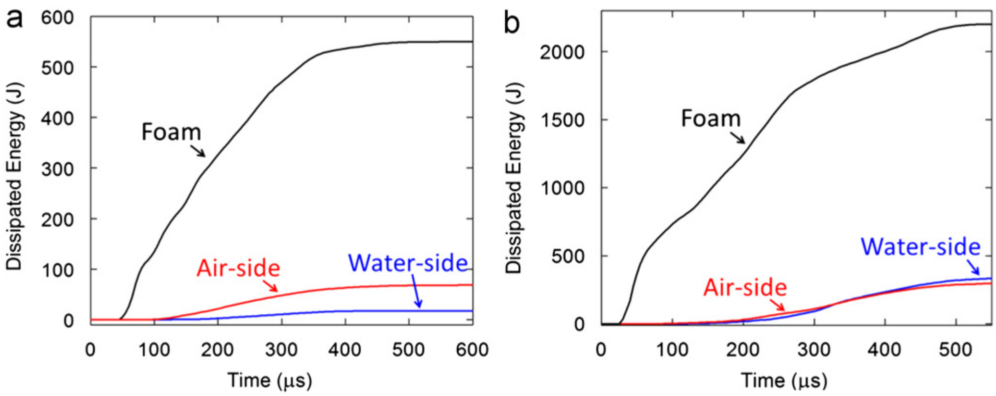

Fig. 18. Energies dissipated in the core and two skins during blast loading in tests ♯2-1 (a) and ♯2-3 (b).

large portion of the energy is dissipated through the core as well. More interestingly, the water-side and air-side face sheets dissipate very similar amounts of energy (Fig. 18b). The percentages of energy dissipated in test ♯2-3 for the water-side face sheet, air-side face sheet, and core are approximately 11.9%, 10.6%, and 77.5%, respectively. Thus, the model reveals that the core is essential for homogenizing the impulses imparted on both skins and to dissipate a significant fraction of the total imparted energy.

4. Conclusion

In this study, we have developed a fluid–structure interaction numerical model using a coupled acoustic-solid technique capable of accurately describing the interaction between water and composite panels. In addition, the FSI model is able to depict the various material deformation and damage mechanisms in monolithic and sandwich composite panels, such as inter-lamina delamination, fiber and matrix damage, and foam crushing. Numerical simulations on *monolithic composite panels* suggest that:

- Inter-lamina delamination is an important material damage mechanism that affects the load distribution in stacked laminates. Because most matrix materials are rate-dependent, the delamination development and propagation is highly affected by strain rate.
- Since the composite fails in a brittle manner, spring back for monolithic panels tends to occur after unloading.

The numerical model also reveals the following unique properties of *sandwich composite panels*:

- When a sandwich panel is subjected a low impulse, core compaction is approximately homogeneous and the two skins and core displace together. More momentum is transmitted to the back-side face sheet compared to the front-side face sheet. Matrix damage is the dominant failure mode in the composite laminates.
- At high impulses, cavitation leads to heterogeneous amounts of core crushing. The panel response can be divided into *four well defined phases* including one associated to water cavity collapse.
- Core crushing helps homogenize the impulses imparted on both skins.
- Shear off is another failure mechanism observed under high impulses, which tends to happen before the core crushes and the laminates undergo stretching.

As pointed out in the discussion of the numerical results, the model slightly over-estimated matrix damage, e.g., in the simulation of test ♯1-3 at the clamped edge, which indicates that strain-rate effects on the mechanical properties of composite laminates need to be accounted for (Hsiao and Daniel, 1998; Hsiao et al., 1999; Daniel et al., 2011). Therefore, formulation and implementation of a new rate-dependent progressive degradation model, to better capture failure in fiber-reinforced composites, is needed and should be the focus of future studies.

Acknowledgments

This research was carried out under the financial support of the Office of Naval Research (ONR) under grant number N00014-08-1-1055. The support and encouragement provided by Dr. Rajapakse through the study is greatly appreciated.

References

Abaqus 6.9-ef online documentation. 2009, Abaqus, Simulia.

Abrate, S., 2005. Impact on Composite Structures. Cambridge University Press.

Abrate, S., 2011. Impact Engineering of Composite Structures. Springer Verlag.

Andrews, E.W., Moussa, N.A., 2009. Failure mode maps for composite sandwich panels subjected to air blast loading. Int. J. Impact Eng. 36 (3), 418–425.

Arora, H., Hooper, P., Dear, J., 2011. Dynamic response of full-scale sandwich composite structures subject to air-blast loading. Composites Part A: Appl. Sci. Manuf. 42 (11), 1651–1662.

Arora, H., Hooper, P., Dear, J., 2012. The effects of air and underwater blast on composite sandwich panels and tubular laminate structures. Exp. Mech. 52 (1), 59–81.

Barenblatt, G.I., 1983. Citation classic – the mathematical-theory of equilibrium cracks in brittle-fracture. Curr. Contents/Eng. Technol. Appl. Sci. (42)., p. 20–20.

Chen, Y., Tong, Z., Hua, H., Wang, Y., Gou, H., 2009. Experimental investigation on the dynamic response of scaled ship model with rubber sandwich coatings subjected to underwater explosion. Int. J. Impact Eng. 36 (2), 318–328.

Compston, P., Jar, P.Y.B., Davies, P., 1998. Matrix effect on the static and dynamic interlaminar fracture toughness of glass-fibre marine composites. Compos. Part B: Eng. 29 (4), 505–516.

Costanzo, F., Walton, J.R., 1997. A study of dynamic crack growth in elastic materials using a cohesive zone model. Int. J. Eng. Sci. 35 (12–13), 1085–1114.

Daniel, I., Werner, B., Fenner, J., 2010. Strain-rate-dependent failure criteria for composites. Compos. Sci. Technol. 71 (3), 357–364.

Daniel, I.M., Ishai, O., Daniel, I., 1994. Engineering Mechanics of Composite Materials, vol. 22. Oxford University Press, New York.

Dear, J., Lee, H., Brown, S., 2005. Impact damage processes in composite sheet and sandwich honeycomb materials. Int. J. Impact Eng. 32 (1), 130–154.

Dear, J.P., Brown, S.A., 2003. Impact damage processes in reinforced polymeric materials. Compos. Part A: Appl. Sci. Manuf. 34 (5), 411–420.

Deshpande, V.S., Fleck, N.A., 2000. Isotropic constitutive models for metallic foams. J. Mech. Phys. Solids 48 (6-7), 1253–1283.

Deshpande, V.S., Fleck, N.A., 2001. Multi-axial yield behaviour of polymer foams. Acta Mater. 49 (10), 1859–1866.

Deshpande, V.S., Fleck, N.A., 2005. One-dimensional response of sandwich plates to underwater shock loading. J. Mech. Phys. Solids 53 (11), 2347–2383.

Dharmasena, K., Queheillalt, D., Wadley, H., Dudt, P., Chen, Y., Knight, D., Evans, A., Deshpande, V., 2010. Dynamic compression of metallic sandwich structures during planar impulsive loading in water. Eur. J. Mech. A/Solids 29 (1), 56–67.

Dugdale, D.S., 1960. Yielding of steel sheets containing slits. J. Mech. Phys. Solids 8 (2), 100–104.

Espinosa, H., Lee, S., Moldovan, N., 2006. A novel fluid structure interaction experiment to investigate deformation of structural elements subjected to impulsive loading. Exp. Mech. 46 (6), 805–824.

Espinosa, H.D., Zavattieri, P.D., 2003. A grain level model for the study of failure initiation and evolution in polycrystalline brittle materials. Part i: Theory and numerical implementation. Mech. Mater. 35 (3-6), 333–364.

Fleck, N.A., Deshpande, V.S., 2004. The resistance of clamped sandwich beams to shock loading. J. Appl. Mech. 71 (3), 386–401.

Gardner, N., Wang, E., Kumar, P., Shukla, A., 2011. Blast mitigation in a sandwich composite using graded core and polyurea interlayer. Exp. Mech., 1–15.

Geubelle, P.H., Baylor, J.S., 1998. Impact-induced delamination of composites: a 2d simulation. Compos. Part B Eng. 29 (5), 589–602.

Glennie, E.B., 1971. Strain-rate dependent crack model. J. Mech. Phys. Solids 19 (5)., p. 255-272.

Hashin, Z., 1980. Failure criteria for unidirectional fiber composites. J. Appl. Mech., 32947, 329.

Hashin, Z., Rotem, A., 1973. A fatigue failure criterion for fiber reinforced materials. J. Compos. Mater. 7 (4), 448–464.

Hoo Fatt, M.S., Palla, L., 2009. Analytical modeling of composite sandwich panels under blast loads. J. Sandwich Struct. Mater. 11 (4), 357–380.

Hoo Fatt, M.S., Surabhi, H., 2012. Blast resistance and energy absorption of foam-core cylindrical sandwich shells under external blast. Compos. Struct.

Hsiao, H., Daniel, I., 1998. Strain rate behavior of composite materials. Compos. Part B: Eng. 29 (5), 521–533.

Hsiao, H., Daniel, I., Cordes, R., 1999. Strain rate effects on the transverse compressive and shear behavior of unidirectional composites. J. Compos. Mater. 33 (17), 1620.

Hutchinson, J.W., Xue, Z.Y., 2005. Metal sandwich plates optimized for pressure impulses. Int. J. Mech. Sci. 47, 545–569.

Lapczyk, I., Hurtado, J.A., 2007. Progressive damage modeling in fiber-reinforced materials. Compos. Part A: Appl. Sci. Manuf. 38 (11), 2333–2341.

Latourte, F., Grégoire, D., Zenkert, D., Wei, X., Espinosa, H.D., 2011. Failure mechanisms in composite panels subjected to underwater impulsive loads. J. Mech. Phys. Solids.

Latourte, F., Wei, X., Feinberg, Z.D., Vaucorbeil, A., Tran, P., Olson, G.B., Espinosa, H.D., 2012. Design and identification of high performance steel alloys for structures subjected to underwater impulsive loading. Int. J. Solids Struct.

Latourte, F., Wei, X., Feinberg, Z.D., de Vaucorbeil, A., Tran, P., Olson, G.B., Espinosa, H.D., 2012. Design and identification of high performance steel alloys for structures subjected to underwater impulsive loading. Int. J.Solids Struct. 49 (13), 1573–1587.

LeBlanc, J., Shukla, A., 2011. Dynamic response of curved composite panels to underwater explosive loading: experimental and computational comparisons. Compos. Struct.

LeBlanc, J., Shukla, A., 2011. Response of e-glass/vinyl ester composite panels to underwater explosive loading: effects of laminate modifications. Int. J. Impact Eng. 38 (10), 796–803.

Lee, D.G., Lim, T.S., Cheon, S.S., 2000. Impact energy absorption characteristics of composite structures. Compos. Struct. 50 (4), 381–390.

Lee, S., Barthelat, F., Hutchinson, J., Espinosa, H., 2006. Dynamic failure of metallic pyramidal truss core materials – experiments and modeling. Int. J. Plasticity 22 (11), 2118–2145.

Liang, Y., Spuskanyuk, A.V., Flores, S.E., Hayhurst, D.R., Hutchinson, J.W., McMeeking, R.M., Evans, A.G., 2007. The response of metallic sandwich panels to water blast. J. Appl. Mech. 74 (1), 81–99.

Massabò, R., Cavicchi, A., 2011. Interaction effects of multiple damage mechanisms in composite sandwich beams subject to time dependent loading. Int. J.Solids Struct.

McShane, G., Deshpande, V., Fleck, N., 2010. Underwater blast response of free-standing sandwich plates with metallic lattice cores. Int. J. Impact Eng. 37 (11), 1138–1149.

Mori, L.F., Lee, S., Xue, Z.Y., Vaziri, A., Queheillalt, D.T., Dharmasena, K.P., Wadley, H.N.G., Hutchinson, J.W., Espinosa, H.D., 2007. Deformation and fracture modes of sandwich structures subjected to underwater impulsive loads. J. Mech. Mater. Struct. 2 (10), 1981–2006.

Mori, L.F., Queheillalt, D.T., Wadley, H.N.G., Espinosa, H.D., 2009. Deformation and failure modes of i-core sandwich structures subjected to underwater impulsive loads. Exp. Mech. 49 (2), 257–275.

Oguni, K., Ravichandran, G., 2001. Dynamic compressive behavior of unidirectional e-glass/vinylester composites. J. Mater. Sci. 36 (4), 831–838.

Porfiri, M. and N. Gupta, A review of research on impulsive loading of marine composites. Major Accomplishments in Composite Materials and Sandwich Structures, 2010: pp. 169–194.

Qiu, X., Deshpande, V.S., Fleck, N.A., 2004. Dynamic response of a clamped circular sandwich plate subject to shock loading. J. Appl. Mech.-Trans. ASME 71 (5), 637–645.

Qiu, X., Deshpande, V.S., Fleck, N.A., 2005. Impulsive loading of clamped monolithic and sandwich beams over a central patch. J. Mech. Phys. Solids 53 (5), 1015–1046.

Rathbun, H., Radford, D., Xue, Z., He, M., Yang, J., Deshpande, V., Fleck, N., Hutchinson, J., Zok, F., Evans, A., 2006. Performance of metallic honeycomb-core sandwich beams under shock loading. Int. J.Solids Struct. 43 (6), 1746–1763.

Roy, R., Sarkar, B., Bose, N., 2001. Impact fatigue of glass fibre-vinylester resin composites. Compos. Part A: Appl. Sci. Manuf. 32 (6), 871–876.

Samudrala, O., Huang, Y., Rosakis, A., 2002. Subsonic and intersonic mode ii crack propagation with a rate-dependent cohesive zone. J. Mech. Phys. Solids 50 (6), 1231–1268.

Tagarielli, V., Deshpande, V., Fleck, N., 2010. Prediction of the dynamic response of composite sandwich beams under shock loading. Int. J. Impact Eng. 37 (7), 854–864.
Tagarielli, V.L., Deshpande, V.S., Fleck, N.A., 2008. The high strain rate response of pvc foams and end-grain balsa wood. Compos. Part B: Eng. 39 (1), 83–91.
Tvergaard, V., Hutchinson, J.W., 1996. Effect of strain-dependent cohesive zone model on predictions of crack growth resistance. Int. J.Solids Struct. 33 (20-22), 3297–3308.
Vaziri, A., Xue, Z., Hutchinson, J., 2006. Metal sandwich plates with polymer foam-filled cores. J. Mech. Mater. Struct. 1 (1), 97–127.
Vaziri, A., Xue, Z.Y., Hutchinson, J.W., 2007. Performance and failure of metal sandwich plates subject to shock loading. J. Mech. Mater. Struct.
Wang, E., Shukla, A., 2011. Blast performance of sandwich composites with in-plane compressive loading. Exp. Mech., 1–10.
Xu, D.B., Hui, C.Y., Kramer, E.J., Creton, C., 1991. A micromechanical model of crack-growth along polymer interfaces. Mech. Mater. 11 (3), 257–268.
Xue, Z.Y., Hutchinson, J.W., 2003. Preliminary assessment of sandwich plates subject to blast loads. Int. J. Mech. Sci. 45 (4), 687–705.
Xue, Z.Y., Hutchinson, J.W., 2004. A comparative study of impulse-resistant metal sandwich plates. Int. J. Impact Eng. 30 (10), 1283–1305.
Zarei, H., Kröger, M., 2008. Optimum honeycomb filled crash absorber design. Mater. Design 29 (1), 193–204.